Revision 2

Incommensurate to normal phase transition in malayaite

Thomas Malcherek[1]*, Michael Fischer[2], Boriana Mihailova[1], Bianca Paulenz[1], Carsten Paulmann[1], Ulrich Bismayer[1]

1) Mineralogisch-Petrographisches Institut, Fachbereich Erdsystemwissenschaften, Universität Hamburg, Grindelallee 48, 20146 Hamburg, Germany
2) Fachbereich Geowissenschaften, Bremen Center for Computational Materials Science, and MAPEX Center for Materials and Processes, Universität Bremen, Bibliothekstraße 1, 28359 Bremen, Germany

*E-mail: thomas.malcherek@uni-hamburg.de

Wordcount: 7392

Pages: 42

36.686

Keywords: phase transition, phonon softening, 1d-modulation, thermal expansion, synchrotron XRD

Abstract

We report variable temperature X-ray diffraction (20 K < T < 295 K) and Raman scattering (90 K < T < 400 K) data of malayaite, the tin analog of the mineral titanite, aided by results from density functional perturbation theory. The phase transition from the normal to the incommensurately modulated crystal structure occurs at $T_c = 50\pm2$ K with an almost constant **q**-vector of $0.27\mathbf{b}^*$. Some first order satellite diffraction maxima are observable up to 55 K, where they increasingly broaden towards the main reflections. Softening of the lowest frequency transverse optical B_g phonon mode, dominated by antiparallel motion of Ca atoms, is observed on cooling from 400 to 90 K. This confirms the displacive character of the transition to the modulated structure, indicated by the instability of this phonon mode in the zero-temperature approximation of first principle computation. The transition to the incommensurately modulated phase is preceded by a temperature region of anomalous thermal expansion in the normal phase, marked by negative thermal expansion along [010] and consequently a change from hardening to softening phonon modes on cooling below 150K. The modulated phase of malayaite highlights the potential of density functional perturbation theory for the discovery of hitherto unknown ground state structures of minerals.

41 ## Introduction

42

43 The fact that crystal structures of minerals can spontaneously change at critical temperatures
44 or pressures is of crucial importance for their physical properties and for the formation of
45 characteristic microstructures. In the process of such displacive phase transitions, commonly
46 the temperature induced motion of atoms, described by the superposition of phonon modes, is
47 partially frozen in. This results in static displacements of atoms away from their average
48 position in the parent phase. It is less well known that the soft phonon modes responsible for
49 displacive phase transitions may generate a distorted phase that destroys the periodicity of the
50 crystal structure in three-dimensional space, giving rise to an aperiodic (or incommensurately
51 modulated) crystal structure. Such a case is presented in the following.
52 Malayaite is the tin analogue of the common accessory mineral titanite, $CaTiSiO_5$
53 (Takenouchi 1971; Higgins and Ribbe 1977). The titanite crystal structure of general formula
54 $AMO'TO_4$ consists of parallel and kinked chains of corner sharing, distorted MO_6 octahedra,
55 laterally connected via isolated TO_4 tetrahedra. The resulting heteropolyhedral framework is
56 charge balanced by A-cations occupying its voids. While A=Ca, M=Sn and T=Si in
57 malayaite, many other cation combinations are known to form the titanite framework. Among
58 these are the minerals of the tilasite (T=As, P, S, V; A=Na, Ca; M=Mg, Al, Ti, Fe^{3+}) and
59 amblygonite (T=P; A=Li, M=Al, Fe^{3+}) groups, where the chain forming oxygen atom O' may
60 be substituted by F^- or $(OH)^-$ for charge balance, as well as the kieserite group minerals
61 (T=As, P; A=□, M= Mn, Fe, Co, Ni, Al, Zn), where O' belongs to a water molecule and the
62 A-site is vacant.
63 The titanite aristotype structure has space group symmetry $C2/c$, often described in an $A2/a$-
64 setting in the literature. Contrary to malayaite, pure titanite distorts to $P2_1/c$ ($P2_1/a$) at
65 temperatures below 493 K (Taylor and Brown 1976), forming a crystal structure with ordered
66 off-center displacements of the Ti cations (Higgins and Ribbe 1976; Speer and Gibbs 1976;

Ghose et al. 1991; Salje et al. 1993; Zhang et al. 1995; Kek et al. 1997; Hayward et al. 2000; Malcherek 2001; Malcherek et al. 2001; Malcherek and Fischer 2018). Isomorphous phase transitions are observed in several isotypic compounds (Malcherek et al. 2004; Malcherek 2007), where the phase transition temperature is proportional to the squared off-center displacement of d^0 transition metal cations Ti, Nb or Ta occupying the M-site. In most natural titanite crystals the macroscopic formation of the ordered titanite structure is suppressed, as these crystals invariably contain considerable concentrations of Al or Fe replacing Ti (Higgins and Ribbe 1976; Oberti et al. 1991), thus diluting the second order Jahn-Teller distortion (Kunz and Brown 1995) and pinning antiphase boundary domain walls (Heurck et al. 1991). Other known distortions of the titanite aristotype structure involve transitions to triclinic symmetry, accompanied by splitting of the M-site into two symmetrically inequivalent sites. While $CaGe_2O_5$ (Aust et al. 1976; Malcherek and Bosenick 2004) or $CaZrGeO_5$ (Malcherek and Ellemann-Olesen 2005) exhibit temperature driven monoclinic-triclinic phase transitions, Ta- and Al-rich natural titanite has been reported with triclinic symmetry as well (Lussier et al. 2009). The nominally Ti-free end member zabińskiite, $Ca(Al_{0.5}Ta_{0.5})(SiO_4)O$ (Pieczka et al. 2017) is equally triclinic. Similarly, the minerals of the amblygonite group have triclinic symmetry (Groat et al. 1990) and at pressures above 4.95 GPa malayaite also adopts triclinic symmetry (Rath et al. 2003). Further, high temperature anomalies have been observed for the malayaite structure (Groat et al. 1996; Meyer et al. 1998; Bismayer et al. 1999), but these do not seem to involve symmetry changes.

Recently the occurrence of a modulated structure in malayaite at 20 K has been reported (Malcherek et al. 2020). With the aim to detect the phase transition to this modulated structure, the present work explores the temperature dependence of the dynamic malayaite crystal structure in the temperature range between 20K and 400K using X-ray diffraction as well as Raman scattering data, aided by ab-initio calculations.

Methods

The investigated malayaite crystals are from the El Hammam mine, Morocco (Sonnet and Verkaeren 1989) as previously described by Malcherek et al. (2020). The average chemical composition has been determined to be $Ca(Sn_{0.97}Ti_{0.03})SiO_5$ by wavelength-dispersive electron microprobe analysis using a Cameca SX100 (supplementary table S1). No significant impurity elements other than Ti are indicated. The small Ti content is inhomogeneously distributed, giving rise to local zonation as evidenced in electron backscattering images (supplementary figure S2).

Single crystal X-ray diffraction at variable temperatures has been conducted in-house, using a Nonius KappaCCD diffractometer with graphite monochromated MoKα radiation, and with synchrotron radiation at beamline P24 of PETRAIII/DESY, Hamburg, Germany. Crystals were cooled using an Oxford Cryostream N_2 cooler and a Cryocool-LT He gas stream cooler respectively. At P24, diffraction data have been collected in ϕ and ω scans at two detector positions on a four-circle kappa diffractometer (EH1) with a wavelength of $\lambda = 0.61992$Å. The beam was monochromated by a water-cooled Si double crystal monochromator. In order to bracket the phase transition temperature, several malayaite crystals were cooled to 20 K, before raising the temperature in steps between diffraction measurements. The final run, which is reported here, involved 2 K temperature steps in the vicinity of the phase transition temperature between 42 and 52 K. Each temperature was allowed to settle for 5 minutes prior to starting the scans. Scattered X-rays have been detected using a Dectris Pilatus 1M CdTe detector at a distance of 150 mm to the crystal. Pixel data have been integrated, corrected and reduced using the Eval15 software package (Schreurs et al. 2010). Reciprocal space reconstructions were calculated using CrysAlisPro (Rigaku Oxford Diffraction 2021). Structure refinement has been performed using Jana2006 (Petříček et al. 2014) with scattering factors for the uncharged atoms. Attempts to refine mixed Sn/Ti occupancy at the M position did only yield Ti site occupancies below the average level indicated by microprobe analysis

(< 0.03 apfu). Full Sn occupancy at the M-site is therefore assumed in the following. A Becker-Coppens model for secondary isotropic extinction of type I with Lorentz distribution of the mosaic blocks (Becker and Coppens 1974) was applied. Refinement results are provided as CIF in Online Materials.

Polarized Raman spectra have been collected using the green line (λ =514.532 nm) of a Coherent Innova 90 C FreD Ar^+ laser in backscattering geometry at temperatures in the range 90 to 400 K, controlled by a Linkam THMS-E600 stage mounted on a Horiba Jobin-Yvon T64000 triple-grating spectrometer equipped with an Olympus BH41 microscope. The instrumental precision in determining the peak position was 0.35 cm^{-1}, with a spectral resolution of 2 cm^{-1}. The temperature run was conducted with [010] parallel to the polarization direction of the incident light ($\mathbf{E}_i$). Parallel polarized ($\mathbf{E}_i$ || to the polarization direction of the scattered light, $\mathbf{E}_s$) and cross polarized ($\mathbf{E}_i \perp \mathbf{E}_s$) spectra have been measured at each temperature step. Data evaluation was performed using IgorPro 9.01. Spectra have been background subtracted, temperature corrected to account for the Bose-Einstein occupation factor and normalized to integrated intensity. Individual Raman signals were fitted using Voigt and Lorentzian peak shapes. Weak Raman scattering signals from rotational modes of N_2, cf. Claps et al. (1999), observable in the wavenumber range below approximately 100 cm^{-1} were included in the peak fitting procedure, in order to accurately describe the low temperature peak profile of the soft-mode near 50 cm^{-1}. An overview of the corrected Raman spectra is shown in the supplementary figure S3.

First principle calculations were performed by means of variational density functional perturbation theory (DFPT) (Gonze 1997; Gonze and Lee 1997) as implemented in the CASTEP computer code (Clark et al. 2005; Refson et al. 2006). These calculations have been described in more detail elsewhere (Malcherek and Fischer 2018; Malcherek et al. 2020). The

plane-wave basis-set cut-off was set to 1200 eV. Norm-conserving pseudopotentials from the Bennett & Rappe pseudopotential library (Bennett 2012), generated using the OPIUM code (Rappe et al. 1990) have been used. An irreducible set of 16 k-points in the Brillouin zone (BZ) has been sampled with a Monkhorst-Pack mesh of 4 x 4 x 3. Exchange-correlation energy contributions have been treated in the generalized gradient (GGA) approximation. The results reported here have been calculated using the PBE flavor of the GGA (Perdew et al. 1996). Phonon calculations were conducted with the zero-pressure optimized crystal structure. Calculations for the base-centered lattice were carried out using the reduced cell, but the results are reported in the conventional C-centered setting, unless otherwise indicated. Raman activities were computed using a hybrid method that combines DFPT with the finite displacement method (Milman et al. 2010), similar to the approach proposed by Porezag and Pederson (1996).

Results and Discussion

Raman scattering

In malayaite 21 Raman active optical modes (9 A_g + 12 B_g) are expected for space group symmetry *C*2/*c*. Figure 1 shows the parallel and cross polarized Raman spectra measured at 90 K in comparison to the DFT-calculated Raman spectrum for random orientation. The calculated spectrum is shown with Lorentzian broadening of 4 cm^{-1} (FWHM) and with wavenumbers multiplied by a factor of 1.04 to account for the volume expansion inherent to the PBE exchange-correlation functional. With this scaling factor the most intense Raman mode at 575 cm^{-1} (#16) coincides with the calculated A_g mode frequency of 552.36 cm^{-1}. Judging by calculated peak position, intensity and symmetry of the Raman modes, all 21 modes can be identified in the experimental spectra (Table 1). With the selected scattering geometry, only A_g modes should be observable in the parallel polarized spectrum, while B_g modes should be observable in the cross polarized spectrum. The intensity of some modes

proved to depend strongly on sample orientation. Thus the intensities of modes 12 and 20 are enhanced in the parallel polarized spectra when rotating the crystal by 90° with respect to $\mathbf{E}_i$, confirming that their symmetry is A_g.

Mode 1 is assigned to the soft-mode, which is unstable in the calculated phonon dispersion (see below and Malcherek et al. (2020)). Softening of this mode is indeed observed for the entire experimentally studied temperature range from 400 K down to 90 K (Figure 2a). The linear mode softening on cooling accelerates at 150 K, where the slope changes from 0.043 cm^{-1}/K to 0.074 cm^{-1}/K. If this linear trend continued, it would extrapolate to 38 cm^{-1} at 0 K. As shown in Figure 2 and in accordance with its B_g symmetry, the mode is dominated by antiparallel motion of the Ca atoms approximately along [001], where each Ca swings with O1 as a pivot. The direction of this pendular motion corresponds to the largest Ca displacement amplitude observed in structure refinements of malayaite (Figure 2b).

Figure 3 shows the temperature evolution of the mode 2 frequency (as wavenumbers, in cm^{-1}), to which antiparallel Ca-motion subparallel [001] contributes, albeit with smaller amplitude than for the soft-mode at lower frequencies. Instead, motion of the chain forming O1 atom and shifting of the SiO_4 tetrahedra parallel [001] contribute more strongly to this phonon mode. Figure 4 shows the respective temperature dependence of mode 5. The Ca vibrations associated with this phonon mode parallel those of the O1 atoms in mode 2. Common to these and many other modes are anomalies in the temperature dependence of their frequency close to 150 K. Softening of mode 1 accelerates below this temperature, while other modes like modes 2 and 5 start to soften below 150 K, after previous, conventional hardening above this temperature. As expected, the frequency changes of the hard modes 2 and 5 are much smaller than that of the soft mode.

Mode 3 at 175 cm^{-1} is an A_g-mode and its temperature evolution differs slightly from the B_g hard modes described above. While this mode also softens on cooling below 150 K, its frequency remains almost constant above that temperature and up to 400 K (Figure 5). The

195 atomic movements associated with this phonon mode involve a shift of the SiO_4-tetrahedron
196 along the y-direction, i.e. parallel to the two-fold rotation axis, as well as a torsional motion of
197 one of the tetrahedral edges. The Ca-O1 bond shifts in the same direction as the Si atom, so
198 that the Ca-Si distance remains nominally constant (Figure 5).
199
200 **X-ray diffraction**
201 Figure 6 shows the temperature variation of the unit cell parameters between room
202 temperature and 20 K. Owing to the very different diffraction conditions for the in-house and
203 the synchrotron diffraction experiments, different malayaite crystals were utilized in the
204 experiments and their corresponding temperature ranges (Table 2). This entails that the unit
205 cell parameters are slightly different for the two measurements and the in-house unit cell
206 parameters have been offset in Figure 6 accordingly and consistently, in order to visualize the
207 common temperature trends in the data. The different crystal sizes and qualities also manifest
208 themselves in the mosaic spread and the observed secondary extinction effects. While the
209 synchrotron data are affected by strong secondary extinction, with the mosaic spread of
210 crystal 1 estimated to only 0.1°, the secondary extinction effects corrected for the larger
211 crystal 2 (estimated mosaic spread 0.6°) measured with the sealed tube radiation source are
212 much smaller.
213 As already indicated in the previous low-temperature experiment (Malcherek et al. 2020), the
214 thermal expansion of malayaite between 20 K and room temperature is rather small. Only the
215 *c*-parameter shows a conventional temperature expansion of about 0.01 Å across the entire
216 observed temperature range of 280 K. Contrary to this, on heating, the *a* and *b* unit-cell
217 parameters are initially almost constant within their measurement uncertainty, with *b* even
218 decreasing on heating to about 180 K. Only above the latter temperature, both cell dimensions
219 start to expand too. This also causes the cell volume to remain constant up to 150 K, with a
220 following expansion by about 0.8 $Å^3$ to room temperature. The 0.00624 $Å^3$/K slope of the line

fit shown in Figure 6e matches the volume expansion evident from Fig. 4e of Groat et al. (1996). The first data points up to 400 K obtained from this graph have been added in Figure 6e. The onset of temperature expansion above 150 K coincides with the temperature anomaly observed in the Raman scattering at 150 K. A further inflection point in the temperature evolution of the unit cell parameters is observed near 50 K, where *a*, *b* and also β start to decrease on further cooling.

As reported by Malcherek et al. (2020), malayaite has a modulated structure at 20 K. The crystal structure can be described in superspace group C2/c(0β0)s0. Structure refinement with this symmetry setting yields the R-factors shown in Table 2. The partial R-factors with respect to the satellite reflections are significantly smaller than for the malayaite crystal studied previously (Malcherek et al. 2020). Likewise, the amplitude of the modulation is larger, which is also evident by the appearance of weak second order satellite maxima (|m| = 2) in the lowest temperature data. At 20 K the number of observed ($I>3\sigma(I)$) satellite maxima with m= -2, 2 is about 50% of the number of m=-1, 1 satellite maxima, but this fraction falls to less than 10% at 42 K. Therefore, between 20 K and 42 K the structure refinements include second order modulation amplitudes as well as first and second order modulation of the anisotropic displacement parameters (adp), amounting to a total of 185 parameters. The inclusion of modulated adps improves the R-factor with respect to the second order satellite maxima, but does not significantly affect the other partial R-factors. Even at 20 K the refined parameter values of the adp-modulations are generally small, within a range of 3σ, with the exception of those affecting U^{33} of the Ca atom. Above 42 K, where the intensity of second-order satellite maxima becomes negligible, 68 parameters were sufficient to refine the modulated crystal structure. In the immediate vicinity of the phase transition to the normal structure at 48, 50, 52 and 55 K, the dynamic displacements of the Sn, Si and O1 atoms had to be restrained to isotropic in order to prevent non-positive-definite anisotropic displacement tensors. At these temperatures the R-factors with respect to the remaining weak satellite

reflections increase significantly, indicating substantial deviations from $C2/c(0\beta0)s0$ symmetry.

Figure 7a shows reconstructed scattering intensity in a section of the *hk*7 plane at 20 K and at three temperatures in the vicinity of the incommensurate to normal (i-n) transition. At 20 K second order satellite maxima with m=2 and m=-2 are observable, which have disappeared at 44 K. Scattering intensity in m=1 and m=-1 satellite positions does not immediately vanish at 50 K, but diffuse scattering is still observable at the position of few satellite reflections. At the same time very weak Bragg scattering at the positions $\bar{2}07$ and 007 is observed at all temperatures in Figure 7a, which should be absent due to the *c*-glide plane.

The amplitude of the statically modulated Ca-displacement resulting from the structure refinements is shown in Figure 8. Figure 8b shows the square of the component amplitude parallel to ***c***. A line-fit to the data points in the range from 38 to 46 K extrapolates to zero at 50 K, yielding the i-n phase transition temperature. As indicated by the finite but small displacement values above this temperature and the remaining intensity of some first order satellite reflections (Figure 7a), precursor effects of the transition appear within a 10 K temperature range above it. The intensity of the forbidden reflection 007 appears to increase above 50 K. A possible explanation for these reflections might involve disorder of the Ca-atoms subparallel to the [001] direction.

The q-vector remains almost constant in the entire temperature range up to the i-n transition temperature (Table 2, Figure 6f). At 20 K it is slightly longer than previously determined ($0.2723(5)\mathbf{b}^*$ compared with $0.2606(8)\mathbf{b}^*$), which is likely related to the smaller amplitude of the modulation in the previously measured crystal (see below). Only above the i-n transition temperature, where the number of observed satellite reflections diminishes sharply, the q-vector shortens significantly before the intensity of the remaining satellite maxima decreases to zero. This is also due to the aforementioned broadening of the satellite reflections towards the position of the main reflections (cf. Figure 7a, 55 K). The length of the q-vector

273 approximately coincides with the calculated 'minimum' of imaginary phonon frequencies
274 along the B_g phonon branch, which is unstable for the entire path between Γ and Y (Figure
275 7b). At the Γ-point this phonon mode corresponds to mode 1 observed in the Raman
276 scattering. Also shown in Figure 7b is the phonon dispersion of the infrared active B_u phonon
277 with LO/TO-splitting on approaching the center of the BZ and instability close to the Y-point
278 at the BZ boundary. For more details regarding the displacements involved in these and other
279 phonon modes and their calculated phonon dispersion see Malcherek et al. (2020).
280 The amplitude of the Ca-displacement as a function of modulation coordinate is shown in
281 Figure 9. The previous determination of this function at 20 K using a different malayaite
282 crystal (Malcherek et al. 2020) matches these results in terms of the phase of the modulation,
283 with positive and negative maxima at t=0.3 and t=0.8 respectively, and also in terms of
284 relation to the displacements of other atoms (not shown in Figure 9), but the amplitude is
285 larger by a factor of 2.5. The larger amplitude in the present study is probably due to the
286 better quality, i.e. smaller mosaic spread of crystal 1, also indicated by the smaller R-factors
287 obtained in the structure refinements and by the absence of second order satellite maxima in
288 the previous measurement. At 52 K the obtained modulation function is phase shifted by
289 180°, clearly indicating the structural difference with respect to the ordered *C*2/*c*(0β0)*s0*
290 structure below the i-n transition temperature.
291 As shown in Figure 10, the dynamic Ca displacement is dominated by the U^{33} component in
292 the direction of the *c*-axis, which steadily decreases from room temperature to 20 K. At 70 K
293 this displacement component is smaller than expected from the linear trend observed down to
294 95 K. With the onset of the i-n transition it drops by about 30% and continues the previous
295 linear decrease within the modulated phase. Even in the modulated phase at 20 K, the
296 dynamic Ca displacement is still significantly anisotropic. The largest eigenvalue of the
297 displacement tensor is almost 4 times larger than the smallest eigenvalue (0.0021, 0.0023,
298 0.0083), with an eigenvector that is 8° inclined with respect to [001].

Due to the larger modulation amplitude, the Ca-O3 distances at 20 K vary between 2.6665(6) and 2.8011(6) Å around an average of 2.7330(6) Å. These distance variations are larger than those obtained from the previously studied crystal (Malcherek et al. 2020) and locally exceed the displacements observed in the high pressure, triclinic phase (Rath et al. 2003; Malcherek et al. 2020).

Thermal expansion and the 150 K anomaly

As is evident from the thermal expansion and the Raman scattering data, the lattice dynamics of malayaite in the normal phase can be divided into a low and a high temperature regime. In the low-temperature regime below 150 K and above the i-n transition, thermal expansion normal to [001] is absent and various phonon modes soften on cooling, while above 150 K malayaite exhibits conventional thermal expansion with all Raman active phonons except modes 1 and 3 softening on heating. Negative thermal expansion as seen along [010] of malayaite between 50 K and 180 K (Figure 6) has also been observed in several kieserite-type compounds (Wildner et al. 2022), where it extends over a wider temperature range. In order to check whether the normal crystal structure is affected by the anomalies seen in the low-temperature regime, third-order anharmonic displacement parameters for the heavier atoms Ca and Si were tentatively included in the refinement. This approach is based on the Gram-Charlier expansion as implemented in the Jana2006 program and adds 4 additional parameters for each of the two atoms (Table 3). Site symmetry of the Sn atom does not permit such third-order tensor elements. Figure 11 shows the resulting joint probability density function (jpdf) of the Ca and Si atoms in layers parallel to (100). As expected, the probability density of the Ca atom is broad and elongated along [001], while it does not drastically differ from the purely harmonic approximation shown in Figure 2b. However, for the Si atom a somewhat unexpected jpdf seems to evolve below 190 K. With falling temperature and rising probability maximum at the center of the distribution, a significant part of the probability density is

extending towards smaller y-coordinates, i.e. closer to the Ca-atom. Some mildly negative and therefore unphysical areas of jpdf far enough from the average Si position are evident. Because of this and because of the small size of the third order tensor elements that barely exceed the 3σ-level (Table *3*), results of these refinements have to be interpreted with caution. But they might indicate that the Si atom dynamically displaces parallel to $[0\bar{1}0]$ in a shallower, anharmonic potential below 190 K. The one particle potentials obtained from the Si jpdf at various temperatures are shown in Figure 12. The potential is nearly harmonic at 295 K, but it becomes increasingly shallow with falling temperature in direction $[0\bar{1}0]$, while it steepens in the opposite direction (where the calculation is however limited by the negative parts of the jpdf).

A reasonable explanation for this behavior is provided by the softening of mode 1 (Figure 2a), which displaces Ca away from the twofold axis with a frequency that is at least a factor of 3.5 smaller than the frequency of mode 3 (Figure 5), or other, higher frequency A_g modes that displace Si along the twofold axis towards the average Ca position. While the amplitude of the anisotropic Ca-displacements decreases with falling temperature (Figure 10), the frequency of these displacements is decreasing as well, so that the probability of Ca being momentarily positioned off the twofold axis can be expected to remain constant or even to increase, a behavior which may also contribute to the observed extinction violations in the *h*0*l*-layer of reciprocal space. This could help to explain the anomalous thermal expansion normal to [001], as the anharmonicity of the potential is going to shift the average position of the SiO_4 tetrahedron towards the average Ca position for larger mode amplitudes, corresponding to higher temperatures, effectively causing the observed negative thermal expansion along [010]. A very similar contraction on heating has been observed for kieserite (Wildner et al. 2022), where the Ca atom is completely absent and the corner oxygen atoms of the SiO_4-tetrahedron are involved in hydrogen bonding instead. Attempts to refine similarly

anharmonic temperature displacements using the synchrotron data collected for crystal 1 below 90 K were unsuccessful, with Si becoming non-positive-definite in this case.

To summarize, the accelerated softening of the B_g soft mode below 150 K and the observed softening of numerous other phonon modes below this temperature can be associated with the anomalous or negative thermal expansion effects observed in the same temperature range. The negative thermal expansion along [010] can be tentatively explained with anharmonic effects induced by the soft phonon mode. Whether these effects also drive the crystal structure into the incommensurate phase is not entirely clear yet.

Implications

In stark contrast to titanite, the ground-state structure of malayaite is controlled by displacements of the A-site cation. This is clearly related to the presence of Ti at the M-site of titanite and the resulting second order Jahn-Teller effect, and its absence in malayaite respectively. Yet it is remarkable that malayaite is driven to an aperiodically ordered structure, rather than to a simpler, triclinically distorted structure, which is observed down to low temperatures in other titanite type minerals such as amblygonite, $LiAlPO_4F$ and montebrasite, $LiAlPO_4OH$ (Groat et al. 2003).

Soft modes that condense at finite wavevectors ($k \neq 0$), shorter than the distance to the Brillouin-Zone boundary, thus resulting in the formation of displacively modulated crystal structures, are not so common in minerals. Salje (2015) lists 26 minerals or synthetic mineral structures with known modulated crystal structures. At the time of writing a search of the ICSD yielded a total of 39 crystal structure data sets of minerals tagged as modulated (of 1040 modulated structures in total). While this list may be incomplete, the number of minerals known to have incommensurately modulated crystal structures is certainly a small percentage of the known mineral species. However, with the growing popularity and feasibility of first principle phonon dispersion calculations, more potentially soft-mode driven phase transitions to modulated

crystal structures in minerals may become known (Caracas and Gonze 2005). As the example of malayaite shows, even small irregularities in the frequency dispersion of low-lying phonon branches may prove indicative of such displacive phase transitions (Malcherek et al. 2020). Whether or not the incommensurately modulated structure of malayaite is preceded by a commensurately modulated (lock-in) structure (Janssen and Janner 1987) at temperatures below 20 K remains to be determined. The constant temperature evolution of the *q*-vector down to this temperature does not provide immediate indication for this. However, the large temperature displacement of the Ca-atom and its anisotropy subparallel to [001] indicates that its position is only loosely constrained by the titanite-framework structure. Even at 20 K, significant anisotropy of the dynamic Ca displacement remains, in spite of its aperiodically ordered distribution and the concomitant reduction of anisotropic temperature displacement. Together with the apparent excess volume at 20 K this indicates a level of structural frustration that is only partially removed by the formation of the modulated structure and may be followed by further anomalies at even lower temperatures. Apart from further structural studies below 20 K, low temperature specific heat measurements may be conducive to explore such properties.

Acknowledgements

Electron microprobe analysis has been conducted by Stefanie Heidrich, with samples prepared by Peter Stutz. We acknowledge DESY (Hamburg, Germany), a member of the Helmholtz Association HGF, for the provision of experimental facilities. Parts of this research were carried out at PETRA III. Beamtime was allocated for proposals I-20200846 and I-20210049. MF gratefully acknowledges funding by the Deutsche Forschungsgemeinschaft (German Research Foundation, DFG) through a Heisenberg fellowship (project no. 455871835).

References cited

Aust, H., Völlenkle, H., and Wittmann, A. (1976) Die Kristallstruktur der Hoch- und der Tieftemperaturform von $CaGe_2O_5$. Zeitschrift für Kristallographie, 144, 82–90.

Becker, P.J., and Coppens, P. (1974) Extinction within the limit of validity of the Darwin transfer equations. I. General formalism for primary and secondary extinction and their applications to spherical crystals. Acta Crystallographica, A30, 129–147.

Bennett, J.W. (2012) Discovery and Design of Functional Materials: Integration of Database Searching and First Principles Calculations. Physics Procedia, 34, 14–23.

Bismayer, U., Zhang, M., Groat, L.A., Salje, E.K.H., and Meyer, H.-W. (1999) The β-γ phase transition in titanite and the isosymmetric analogue in malayaite. Phase Transitions, 68, 545–556.

Caracas, R., and Gonze, X. (2005) First-principle study of materials involved in incommensurate transitions. Zeitschrift für Kristallographie - Crystalline Materials, 220, 511–520.

Claps, R., Sabbaghzadeh, J., and Fink, M. (1999) Raman Spectroscopy with a Single-Frequency, High-Power, Broad-Area Laser Diode. Applied Spectroscopy, 53, 491–496.

Clark, S.J., Segall, M.S., Pickard, C.J., Hasnip, P.J., Probert, M.I.J., Refson, K., and Payne, M.C. (2005) First principles methods using CASTEP. Zeitschrift für Kristallographie, 220, 567–570.

Ghose, S., Ito, Y., and Hatch, D.M. (1991) Paraelectric-Antiferroelectric Phase Transition in Titanite, $CaTiSiO_5$. I. A high temperature X-ray diffraction study of the order parameter and transition mechanism. Physics and Chemistry of Minerals, 17, 591–603.

Gonze, X. (1997) First-principles responses of solids to atomic displacements and homogeneous electric fields: Implementation of a conjugate-gradient algorithm. Physical Review B, 55, 10337–10354.

Gonze, X., and Lee, C. (1997) Dynamical matrices, Born effective charges, dielectric permittivity tensors, and interatomic force constants from density-functional perturbation theory. Physical Review B, 55, 10355–10368.

Groat, L.A., Raudsepp, M., Hawthorne, F.C., Ercit, T.S., Sherriff, B.L., and Hartman, J.S. (1990) The amblygonite-montebrasite series: Characterization by single-crystal structure refinement, infrared spectroscopy, and multinuclear MAS-NMR spectroscopy. American Mineralogist, 75, 992–1008.

Groat, L.A., Kek, S., Bismayer, U., Schmidt, C., Krane, H.G., Meyer, H., Nistor, L., and Tendeloo, G.V. (1996) A synchrotron radiation, HRTEM, X-ray powder diffraction, and Raman spectroscopic study of malayaite, $CaSnSiO_5$. American Mineralogist, 81, 595–602.

Groat, L.A., Chakoumakos, B.C., Brouwer, D.H., Hoffman, C.M., Fyfe, C.A., Morell, H., and Schultz, A.J. (2003) The amblygonite ($LiAlPO_4F$)-montebrasite ($LiAlPO_4OH$) solid solution: A combined powder and single-crystal neutron diffraction and solid-state ^6Li MAS, CP MAS, and REDOR NMR study. American Mineralogist, 88, 195–210.

Hayward, S.A., Cerro, J. del, and Salje, E.K.H. (2000) Antiferroelectric phase transition in titanite: Excess entropy and short range order. American Mineralogist, 85, 557–562.

Heurck, C.V., Tendeloo, G.V., Ghose, S., and Amelinckx, S. (1991) Paraelectric-Antiferroelectric Phase Transition in Titanite, $CaTiSiO_5$. Physics and Chemistry of Minerals, 17, 604–610.

Higgins, J.B., and Ribbe, P.H. (1976) The crystal chemistry and space group of natural and synthetic titanites. American Mineralogist, 61, 878–888.

——— (1977) The structure of malayaite, $CaSnOSiO_4$, a tin analog of titanite. American Mineralogist, 62, 801–806.

Janssen, T., and Janner, A. (1987) Incommensurability in crystals. Advances in Physics, 36, 519–624.

Kek, S., Aroyo, M., Bismayer, U., Schmidt, C., Eichhorn, K., and Krane, H.G. (1997) The two-step phase transition of titanite, $CaTiSiO_5$: A synchrotron radiation study. Zeitschrift für Kristallographie, 212, 9–19.

Kunz, M., and Brown, I.D. (1995) Out-of-Center Distortions around octahedrally coordinated d^0 transition metals. Journal of Solid State Chemistry, 115, 395–406.

Lussier, A.J., Cooper, M.A., Hawthorne, F.C., and Kristiansen, R. (2009) Triclinic titanite from the Heftetjern granitic pegmatite, Tordal, southern Norway. Mineralogical Magazine, 73, 709–722.

Malcherek, T. (2001) Spontaneous strain in synthetic titanite, $CaTiOSiO_4$. Mineralogical Magazine, 65, 709–715.

——— (2007) A structural phase transition in $NaTaOGeO_4$ and its relation to phase transitions in titanite. Acta Crystallographica, B63, 545–550.

Malcherek, T., and Bosenick, A. (2004) Structure and phase transition of $CaGe_2O_5$ revisited. Physics and Chemistry of Minerals, 31, 224–231.

Malcherek, T., and Ellemann-Olesen, R. (2005) $CaZrGeO_5$ and the triclinic instability of the titanite structure type. Zeitschrift für Kristallographie, 220, 712–716.

Malcherek, T., and Fischer, M. (2018) Phase transitions of titanite $CaTiSiO_5$ from density functional perturbation theory. Physical Review Materials, 2, 023602.

Malcherek, T., Paulmann, C., Domeneghetti, M.C., and Bismayer, U. (2001) Diffuse scattering anisotropy and the $P2_1/a$ <-> A2/a phase transition in titanite, $CaTiOSiO_4$. Journal of Applied Crystallography, 34, 108–113.

Malcherek, T., Bosenick, A., Cemič, L., Fechtelkord, M., and Guttzeit, A. (2004) Isomorphy of structural phase transitions in $LiTaOSiO_4$, $LiTaOGeO_4$ and titanite, $CaTiOSiO_4$. Journal of Solid State Chemistry, 177, 3254–3262.

Malcherek, T., Paulenz, B., Fischer, M., and Paulmann, C. (2020) The modulated low-temperature structure of malayaite, $CaSnOSiO_4$. Acta Crystallographica, B76, 316–

321.

Meyer, H.-W., Bismayer, U., Adiwidjaja, G., Zhang, M., Nistor, L., and Tendeloo, G.V. (1998) Natural titanite and malayaite: structural investigations and the 500K anomaly. Phase Transitions, 67, 27–49.

Milman, V., Refson, K., Clark, S.J., Pickard, C.J., Yates, J.R., Gao, S.-P., Hasnip, P.J., Probert, M.I.J., Perlov, A., and Segall, M.D. (2010) Electron and vibrational spectroscopies using DFT, plane waves and pseudopotentials: CASTEP implementation. Journal of Molecular Structure: THEOCHEM, 954, 22–35.

Oberti, R., Smith, D.C., Rossi, G., and Caucia, F. (1991) The crystal chemistry of high-aluminium titanites. European Journal of Mineralogy, 3, 777–792.

Perdew, J.P., Burke, K., and Ernzerhof, M. (1996) Generalized gradient approximation made simple. Physical Review Letters, 77, 3865–3868.

Petříček, V., Dušek, M., and Palatinus, L. (2014) Crystallographic Computing System JANA2006: General features. Zeitschrift für Kristallographie, 229, 345–352.

Pieczka, A., Hawthorne, F.C., Ma, C., Rossman, G.R., Szełek, E., Szuszkiewicz, A., Turniak, K., Nejbert, K., Ilnicki, S.S., Buffat, P., and Rutkowski, B. (2017) Żabińskiite, ideally $Ca(Al_{0.5}Ta_{0.5})(SiO_4)O$, a new mineral of the titanite group from the Piława Górna pegmatite, the Góry Sowie Block, southwestern Poland. Mineralogical Magazine, 81, 591–610.

Porezag, D., and Pederson, M.R. (1996) Infrared intensities and Raman-scattering activities within density-functional theory. Physical Review B, 54, 7830–7836.

Rappe, A.M., Rabe, K.M., Kaxiras, E., and Joannopoulos, J.D. (1990) Optimized pseudopotentials. Physical Review B, 41, 1227–1230.

Rath, S., Kunz, M., and Miletich, R. (2003) Pressure-induced phase transition in malayaite, $CaSnOSiO_4$. American Mineralogist, 88, 293–300.

Refson, K., Tulip, P.R., and Clark, S.J. (2006) Variational density functional perturbation

theory for dielectrics and lattice dynamics. Physical Review B, 73, 155114.

Rigaku Oxford Diffraction (2021) CrysAlisPro Software system version 171.41.21a. Rigaku Oxford Diffraction, Oxford, UK.

Salje, E.K.H. (2015) Modulated minerals as potential ferroic materials. Journal of Physics: Condensed Matter, 27, 305901.

Salje, E.K.H., Schmidt, C., and Bismayer, U. (1993) Structural Phase Transition in Titanite, $CaTiSiO_5$: A Ramanspectroscopic Study. PCM, 19, 502–506.

Schreurs, A.M.M., Xian, X., and Kroon-Batenburg, L.M.J. (2010) EVAL15: a diffraction data integration method based on ab initio predicted profiles. Journal of Applied Crystallography, 43, 70–82.

Sonnet, P.M., and Verkaeren, J. (1989) Scheelite-, malayaite-, and axinite-bearing skarns from El Hammam, central Morocco. Economic Geology, 84, 575–590.

Speer, J.A., and Gibbs, G.V. (1976) The crystal structure of synthetic titanite, $CaTiOSiO_4$, and the domain texture of natural titanites. American Mineralogist, 61, 238–247.

Takenouchi, S. (1971) Hydrothermal synthesis and consideration of the genesis of malayaite. Mineralum Deposita, 6, 335–347.

Taylor, M., and Brown, G.E. (1976) High-temperature structural study of the $P2_1/a$ <-> A2/a phase transition in synthetic titanite, $CaTiSiO_5$. American Mineralogist, 61, 435–447.

Wildner, M., Zakharov, B.A., Bogdanov, N.E., Talla, D., Boldyreva, E.V., and Miletich, R. (2022) Crystallography relevant to Mars and Galilean icy moons: crystal behavior of kieserite-type monohydrate sulfates at extraterrestrial conditions down to 15 K. IUCrJ, 9, 194–203.

Zhang, M., Salje, E.K.H., Bismayer, U., Unruh, H.-G., Wruck, B., and Schmidt, C. (1995) Phase Transition(s) in titanite $CaTiSiO_5$: An infrared spectroscopic, dielectric response and heat capacity study. Physics and Chemistry of Minerals, 22, 41–49.

571

Mode No.	Irrep (C2/c)	$\bar{\nu}_{calc}$ (cm^{-1})	$\bar{\nu}_{90K}$ (cm^{-1})
1	B_g	-31.36	44.93(4)
2	B_g	126.18	136.88(1)
3	A_g	159.91	173.54(9)
4	B_g	164.19	181.59(6)
5	B_g	198.39	224.77(5)
6	B_g	265.66	291.72(10)
7	A_g	279.72	298.50(42)
8	B_g	282.76	305.62(15)
9	A_g	309.03	324.89(2)
10	B_g	338.60	345.73(10)
11	A_g	335.32	364.67(6)
12	A_g	440.55	447.14(14)
13	A_g	503.47	508.59(23)
14	B_g	513.87	516.23(4)
15	B_g	533.01	542.82(14)
16	A_g	552.36	574.96(1)
17	B_g	721.04	747.39(7)
18	B_g	817.11	853.97(7)
19	A_g	828.24	872.38(7)
20	A_g	859.48	896.24(27)
21	B_g	913.49	966.70(7)

572 Table 1: Calculated and observed Raman mode frequencies (as wavenumbers).

This is the peer-reviewed, final accepted version for American Mineralogist, published by the Mineralogical Society of America.
The published version is subject to change. Cite as Authors (Year) Title. American Mineralogist, in press.
DOI: https://doi.org/10.2138/am-2023-9063. http://www.minsocam.org/

T (K)	a (Å)	b (Å)	c (Å)	β (°)	V(Å^3)	q_y (**b***)	R_{obs} ($I_{obs}>3\sigma(I_{obs})$) N_{main}	N_{1st}	N_{2nd}	GoF	n_p
Crystal 1											
20	6.6628(5)	8.8874(5)	7.1401(6)	113.379(6)	388.10(4)	0.2723(5)	3.28	2.81	3.64	1.08	185
							1228	2394	1045		
30	6.6630(3)	8.8877(5)	7.1405(6)	113.382(3)	388.12(4)	0.2722(5)	3.27	2.74	4.43	1.02	185
							1227	2383	878		
38	6.6634(4)	8.8884(6)	7.1402(5)	113.385(4)	388.16(3)	0.2723(6)	3.58	2.91	6.69	0.97	185
							1221	2332	558		
42	6.6639(5)	8.8895(4)	7.1434(5)	113.389(5)	388.39(3)	0.2712(6)	3.04	2.91	9.58	0.94	185
							1221	2152	151		
44	6.6645(3)	8.8894(5)	7.1418(5)	113.388(3)	388.34(3)	0.2715(4)	3.19	3.01		0.92	68
							1220	2119			
46	6.6636(4)	8.8887(5)	7.1422(6)	113.391(3)	388.26(4)	0.2712(5)	3.15	3.53		0.83	68
							1200	1974			
48	6.6643(3)	8.8892(5)	7.1423(6)	113.392(3)	388.33(4)	0.2710(4)	3.82	5.65		1.27	57
							1196	1833			
50	6.6642(3)	8.8891(5)	7.1422(5)	113.390(3)	388.32(4)	0.2706(5)	3.34	5.93		1.04	57
							1203	1783			
52	6.6638(4)	8.8884(6)	7.1410(4)	113.397(4)	388.19(4)	0.2700(8)	3.34	8.74		1.10	57
							1210	1258			
55	6.6636(3)	8.8893(6)	7.1413(5)	113.394(4)	388.24(4)	0.2659(13)	3.36	8.81		1.0	57
							1180	765			
60	6.6627(5)	8.8885(7)	7.1415(7)	113.395(4)	388.16(5)		3.17			1.04	41
							1219				
70	6.6630(5)	8.8879(8)	7.1411(8)	113.394(5)	388.13(6)		3.09			1.0	41
							1217				
295	6.6652(6)	8.8917(8)	7.1498(13)	113.352(8)	389.02(8)		3.08			1.03	41
							1268				
Crystal 2											

95	6.6607(9)	8.8832(11)	7.1382(9)	113.412(11)	387.58(7)	1.2 771	1.03	41
120	6.6594(10)	8.8826(13)	7.1394(9)	113.396(13)	387.59(7)	1.28 771	1.06	41
150	6.6593(10)	8.8812(13)	7.1402(10)	113.395(11)	387.57(8)	1.16 785	1.06	41
190	6.6596(11)	8.8804(8)	7.1425(10)	113.347(12)	387.82(8)	1.19 787	1.08	41
230	6.6614(10)	8.8841(9)	7.1436(8)	113.358(9)	388.12(6)	1.66 733	1.14	41
295	6.6632(6)	8.8859(6)	7.1458(6)	113.343(5)	388.46(4)	1.18 797	0.98	41

573 Table 2: Unit cell parameters and refinement details.

574

T	R_{obs}	C^{112} ($\cdot 10^{-4}$)		C^{123}($\cdot 10^{-4}$)		C^{222}($\cdot 10^{-4}$)		C^{233}($\cdot 10^{-4}$)	
(K)	($I_{obs}>3\sigma(I_{obs})$)	Ca	Si	Ca	Si	Ca	Si	Ca	Si
95	1.08	2.6(1.9)	3(3)	-1.5(1.4)	1.1(1.8)	-1.2(1.6)	-5(2)	5.3(1.9)	2(2)
120	1.18	1(2)	4(3)	-2.2(1.5)	1.6(1.9)	-1.2(1.6)	-3(2)	7(2)	2(2)
150	1.05	0.2(1.9)	5(3)	-2.4(1.4)	3.2(1.8)	-2.5(1.5)	-3(2)	7.5(1.9)	2(2)
190	1.08	2.1(1.9)	4(3)	-2.6(1.4)	2.3(1.7)	-2.1(1.6)	-2(2)	11(2)	0(2)
230	1.47	7(2)	8(3)	-2.5(1.8)	2(2)	2.3(1.7)	-2.0(1.9)	20(3)	2(2)
295	1.00	1.5(1.6)	5(2)	3.4(1.3)	2.8(1.6)	0.4(1.4)	4.5(1.9)	15.7(1.8)	2(2)

575 Table 3: Refinement results with anharmonic displacement factors

576

577

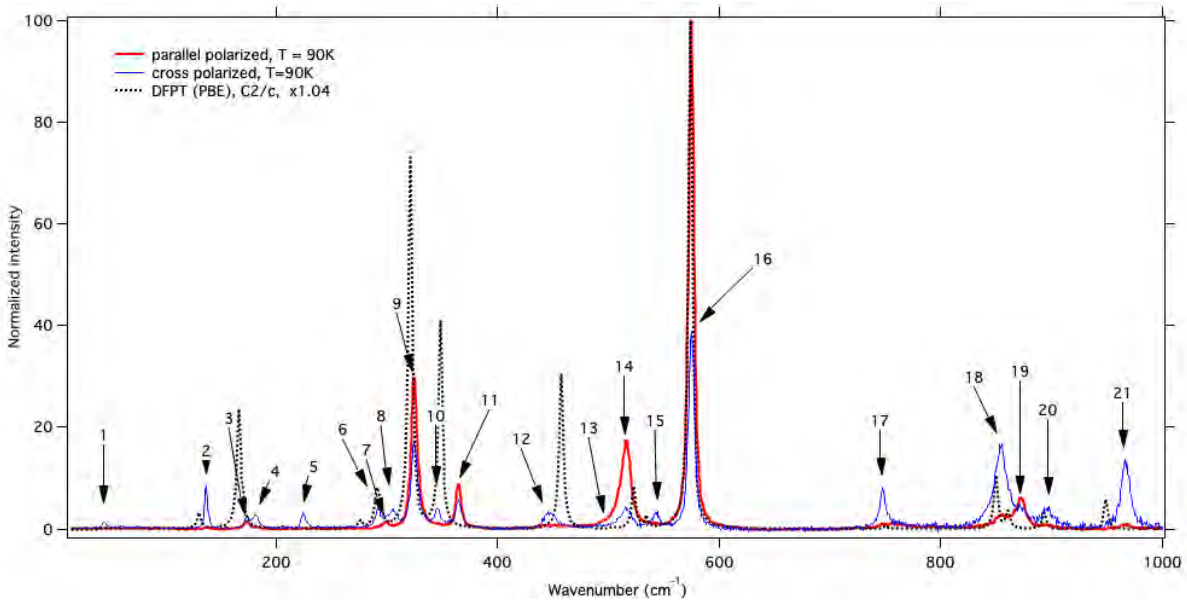

578

579 Figure 1: Observed Raman spectra at 90 K (red and blue lines) and calculated Raman

580 spectrum from DFPT, shifted by a factor of 1.04 (dotted). Observed modes are sequentially

581 numbered from low to high wavenumbers. Cf. Table 1 for peak assignments.

582

This is the peer-reviewed, final accepted version for American Mineralogist, published by the Mineralogical Society of America.
The published version is subject to change. Cite as Authors (Year) Title. American Mineralogist, in press.
DOI: https://doi.org/10.2138/am-2023-9063. http://www.minsocam.org/

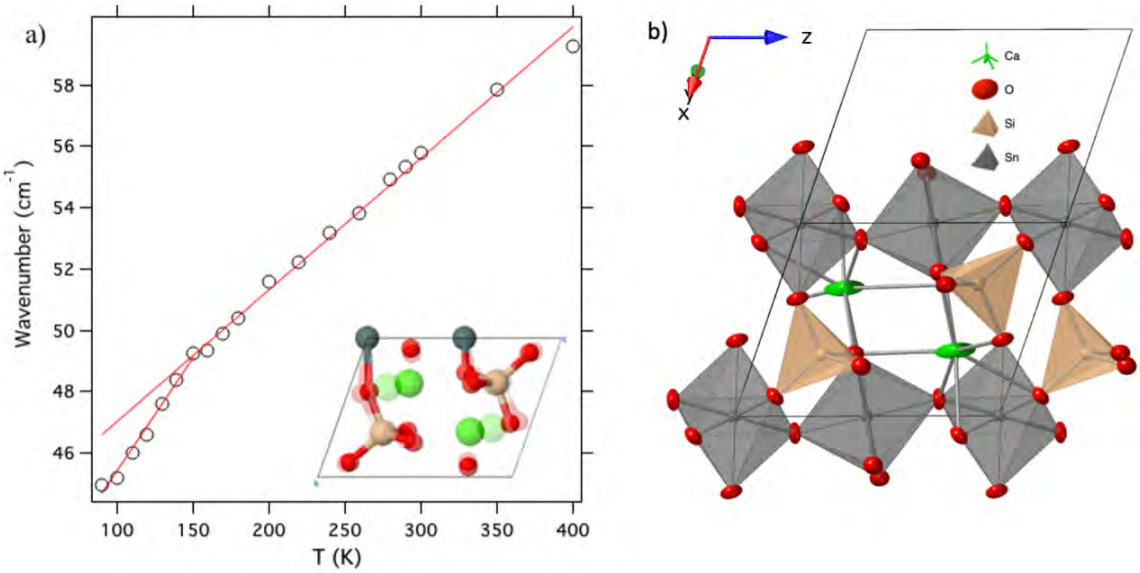

583

584

585 Figure 2: a) Frequency of mode 1 (B_g symmetry). Errors obtained from profile fitting are
586 smaller than the symbol size. The inset pictures two extremal positions of the associated
587 atomic vibrations as obtained by DFPT. Their amplitude is fivefold exaggerated for clarity.
588 The unit cell outline corresponds to the reduced cell. b) The experimentally determined
589 malayaite crystal structure at room temperature (cryst. 1, this work) in the same orientation as
590 in a), with harmonic displacement ellipsoids at the 95% probability level.

591

592

This is the peer-reviewed, final accepted version for American Mineralogist, published by the Mineralogical Society of America.
The published version is subject to change. Cite as Authors (Year) Title. American Mineralogist, in press.
DOI: https://doi.org/10.2138/am-2023-9063. http://www.minsocam.org/

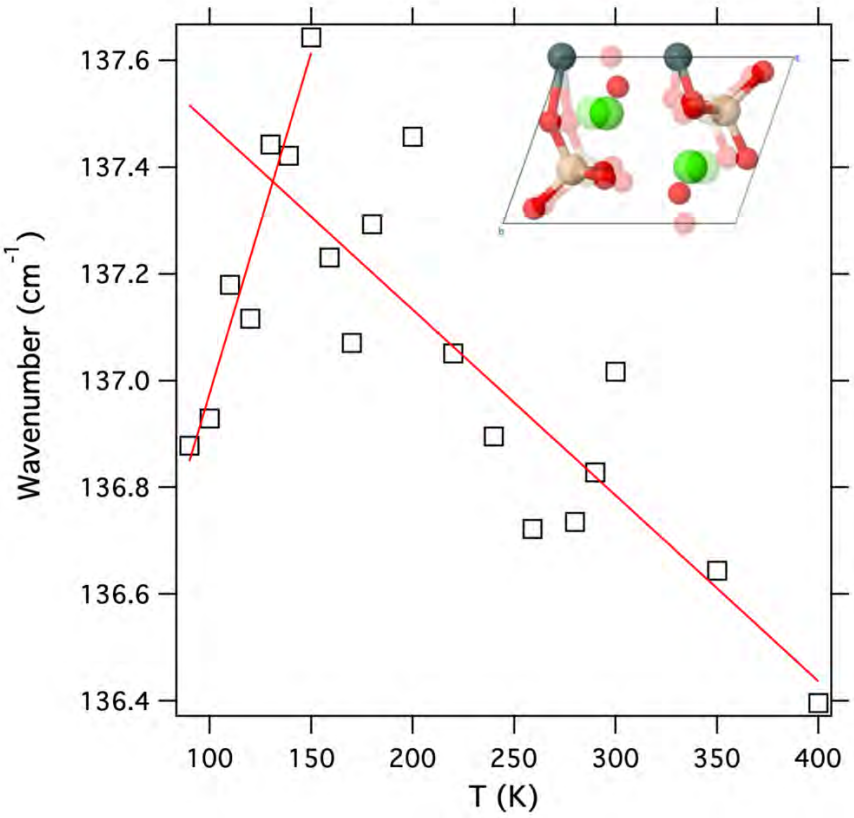

Figure 3: Frequency of Mode 2. Errors obtained from profile fitting are in the order of the symbol size. The inset pictures two extremal positions of the associated atomic vibrations, with fivefold exaggerated amplitude.

598

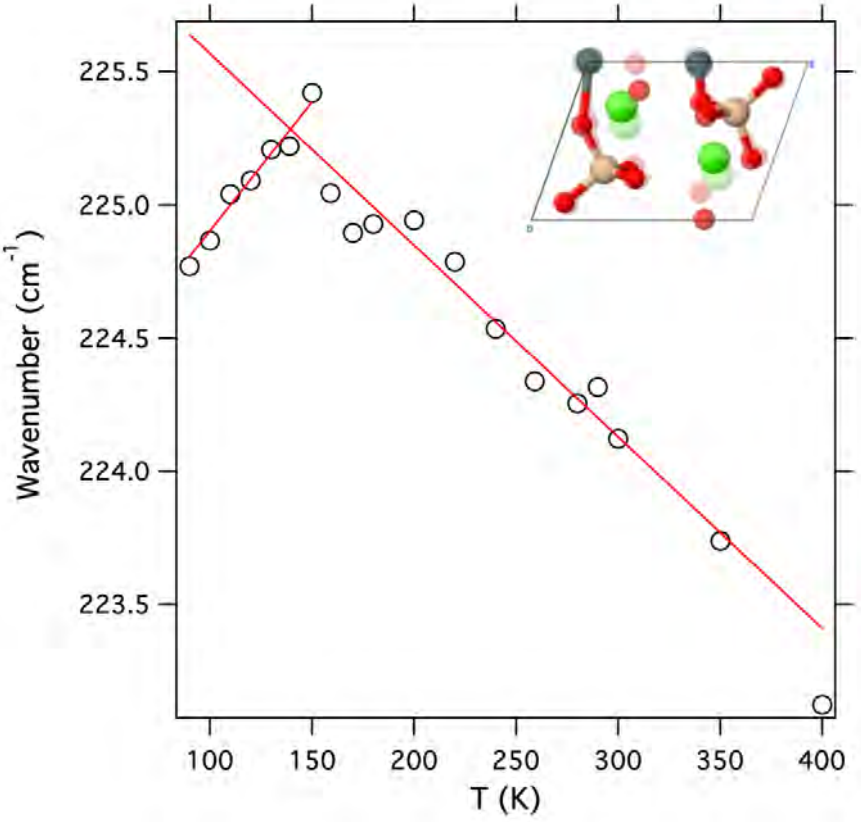

599 Figure 4: Frequency of mode 5. Errors obtained from profile fitting are in the order of the
600 symbol size. The inset pictures two extremal positions of the associated atomic vibrations,
601 with fivefold exaggerated amplitude.

602

This is the peer-reviewed, final accepted version for American Mineralogist, published by the Mineralogical Society of America.
The published version is subject to change. Cite as Authors (Year) Title. American Mineralogist, in press.
DOI: https://doi.org/10.2138/am-2023-9063. http://www.minsocam.org/

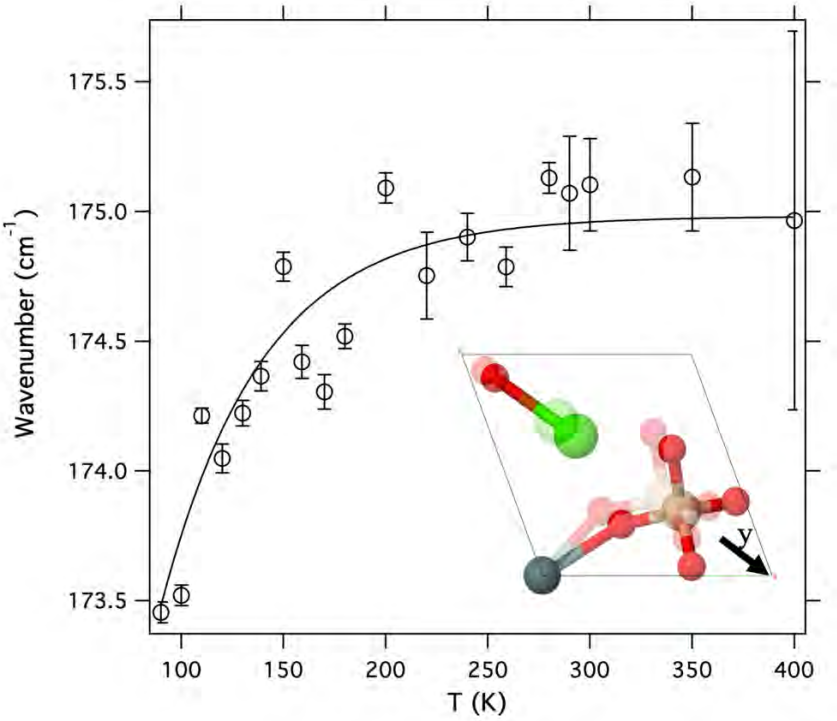

Figure 5: Frequency of mode 3. The inset pictures two extremal positions of the associated atomic vibrations in projection along [001] (fivefold exaggerated amplitude). The unit cell outline corresponds to the reduced cell.

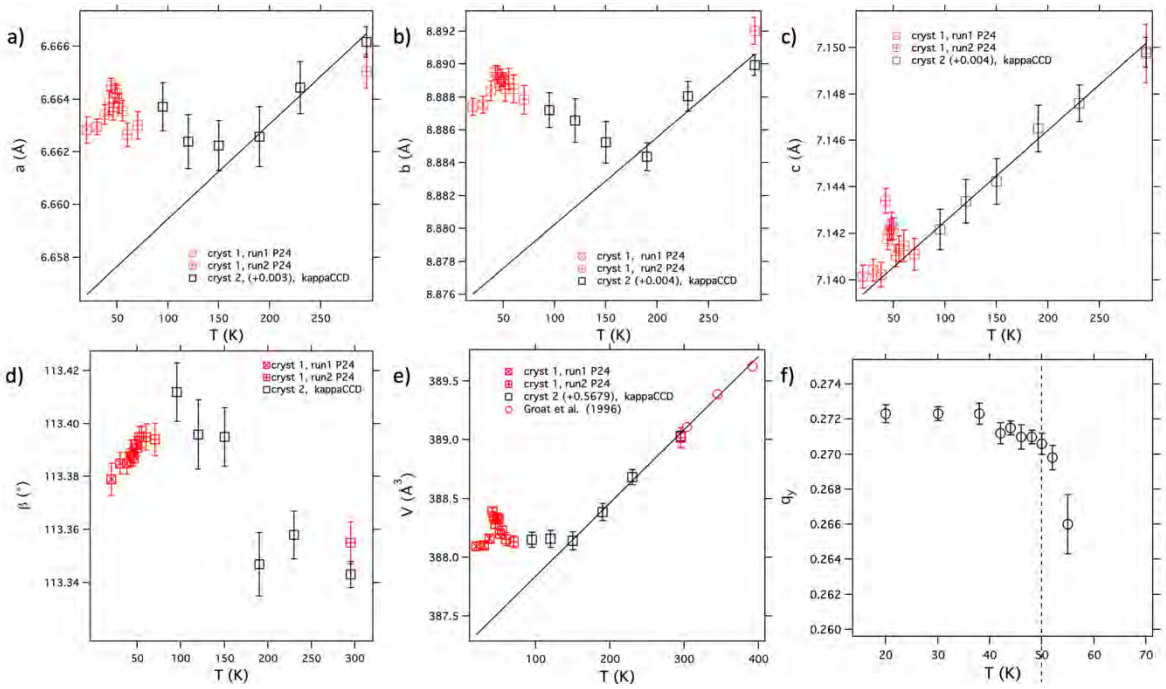

Figure 6: Temperature evolution of unit cell parameters and *q*-vector of malayaite. Cell constants *a*, *b*, *c* and *V* obtained for cryst 2 have been offset in the diagrams to match those of cryst 1. Lines extrapolate the high temperature (T>150K) behavior of cryst 2.

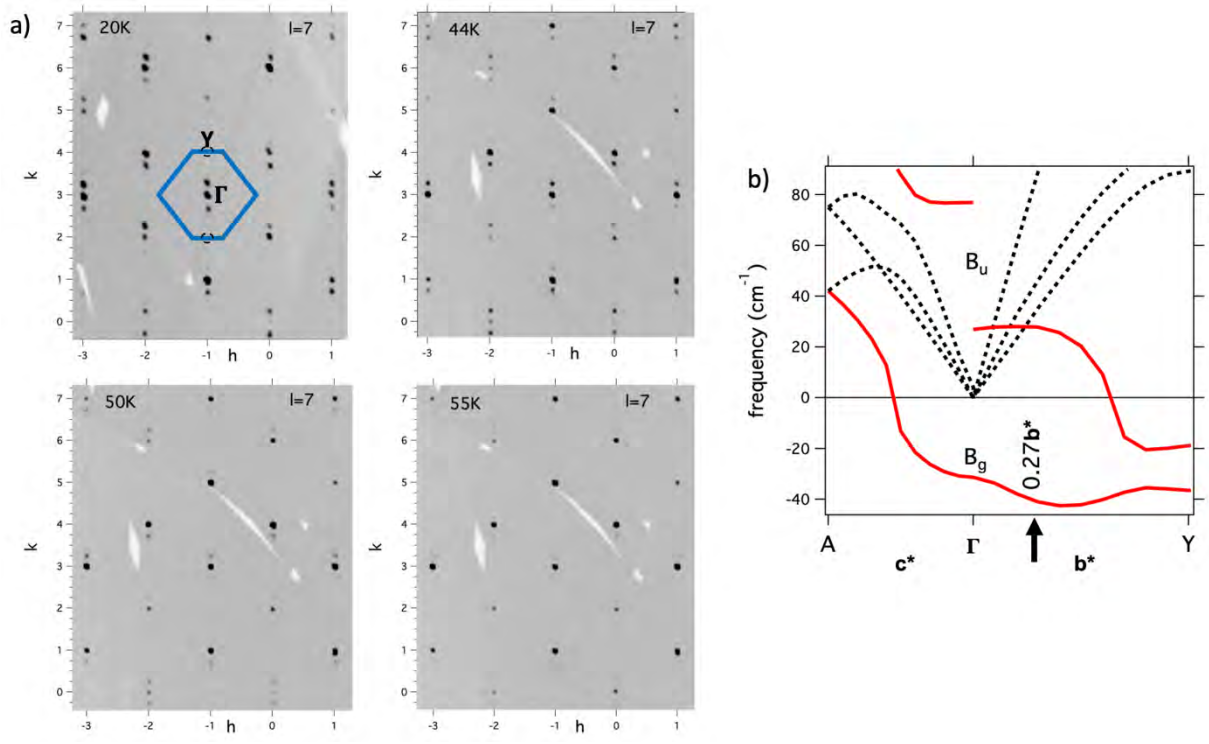

Figure 7: a) reconstructed scattering intensity in the *hk*7 layer at temperatures 20 K, 44 K, 50 K and 55 K. The blue outline indicates the first BZ boundary relative to the $\bar{1}$ 3 7 reciprocal lattice point. b) Calculated phonon dispersion parallel c* and b* for wavenumbers below 90 cm^{-1}. Imaginary frequencies are shown in the real negative wavenumber range. Optical phonon branches are plotted solid (red). Acoustic phonon branches are dashed (black). The observed q-vector is indicated by an arrow.

This is the peer-reviewed, final accepted version for American Mineralogist, published by the Mineralogical Society of America.
The published version is subject to change. Cite as Authors (Year) Title. American Mineralogist, in press.
DOI: https://doi.org/10.2138/am-2023-9063. http://www.minsocam.org/

623

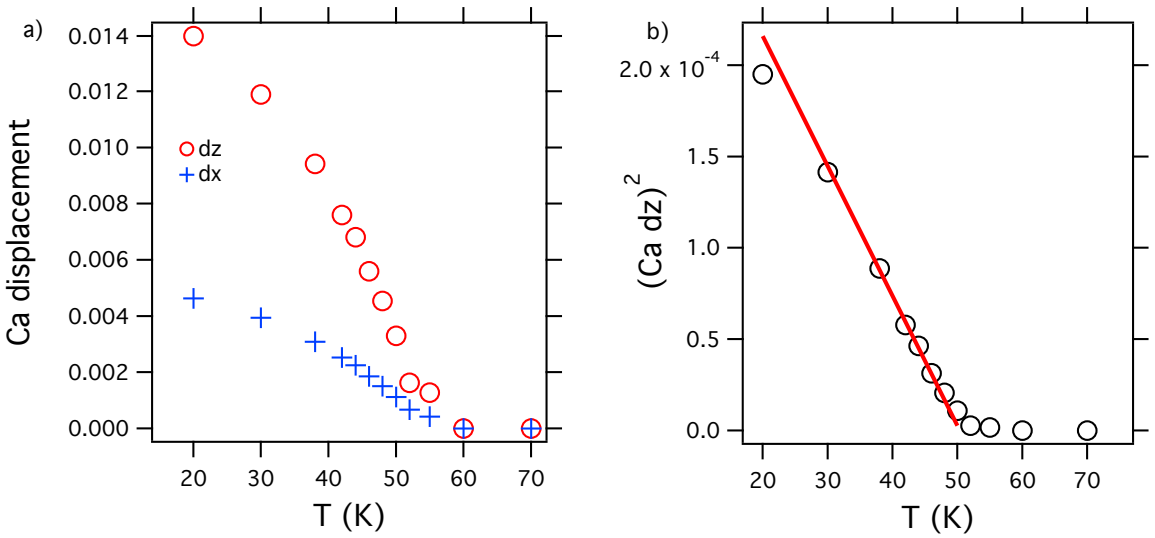

624

625

626 Figure 8: a) Modulation amplitude of Ca displacement parallel **a** (dx) and **c** (dz). b) squared
627 Ca-displacement amplitude parallel **c**. The line has been fitted to the points in the temperature
628 range 38 to 46K.

629

630

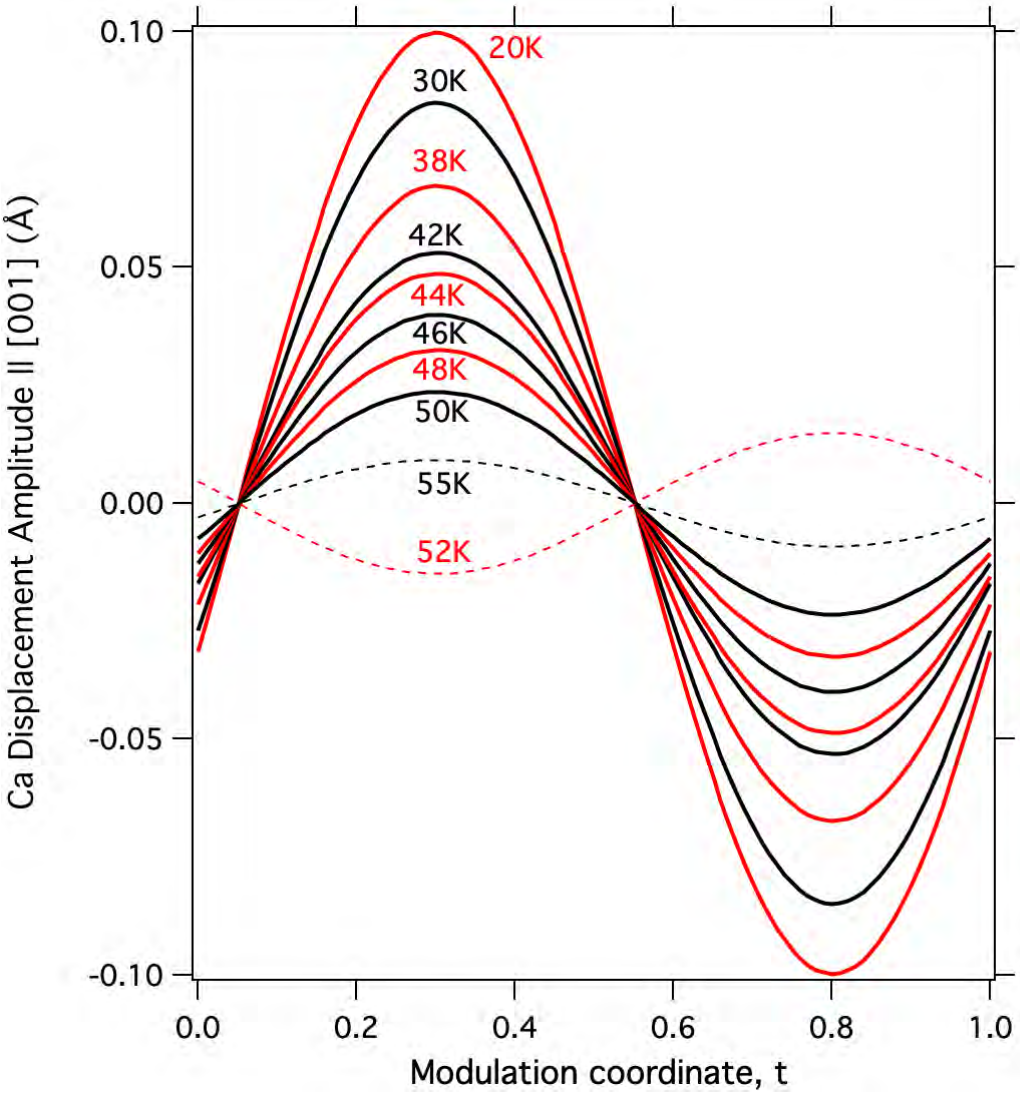

631

632

633 Figure 9: Refined modulation amplitude of the Ca-atom along [001] for different

634 temperatures.

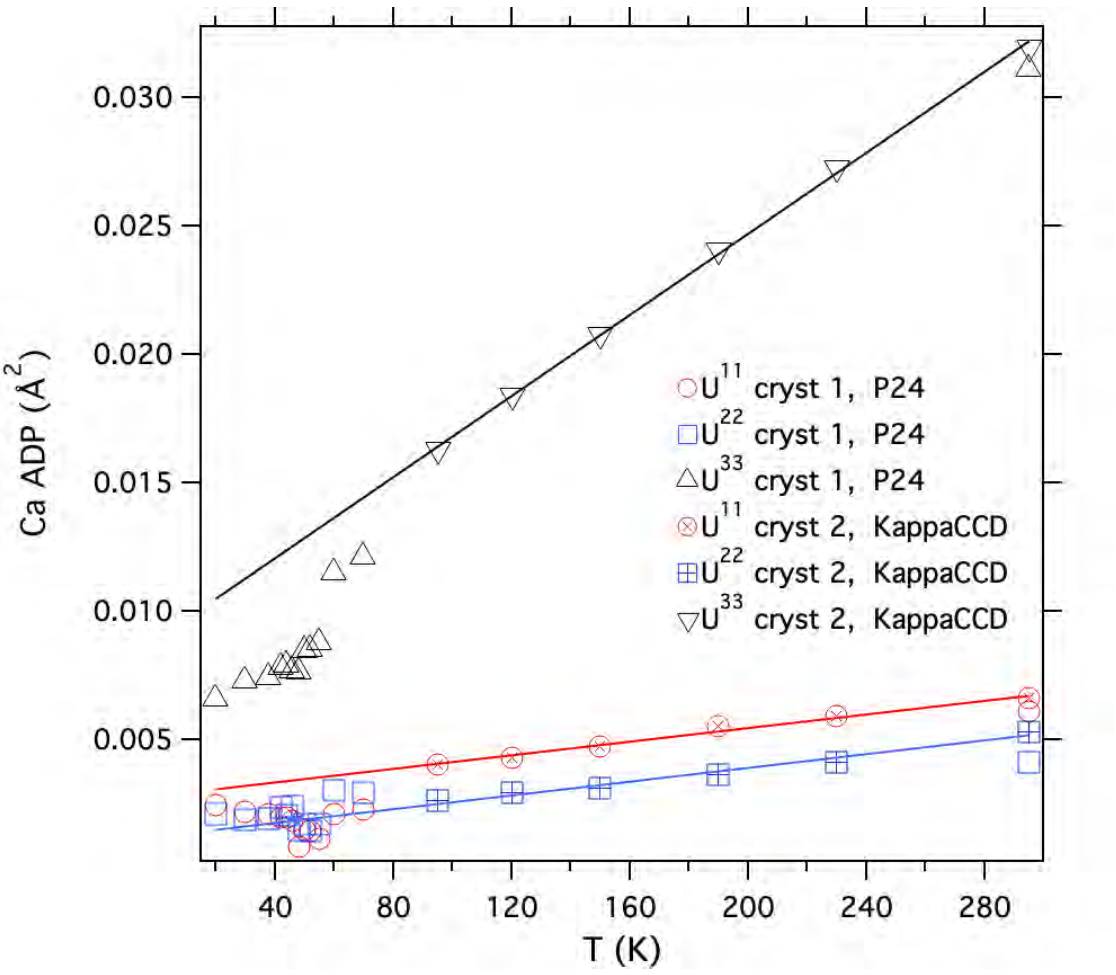

Figure 10: Anisotropic, harmonic displacement parameters for the Ca atom as a function of temperature. Straight lines have been fitted to the data of cryst 2.

This is the peer-reviewed, final accepted version for American Mineralogist, published by the Mineralogical Society of America.
The published version is subject to change. Cite as Authors (Year) Title. American Mineralogist, in press.
DOI: https://doi.org/10.2138/am-2023-9063. http://www.minsocam.org/

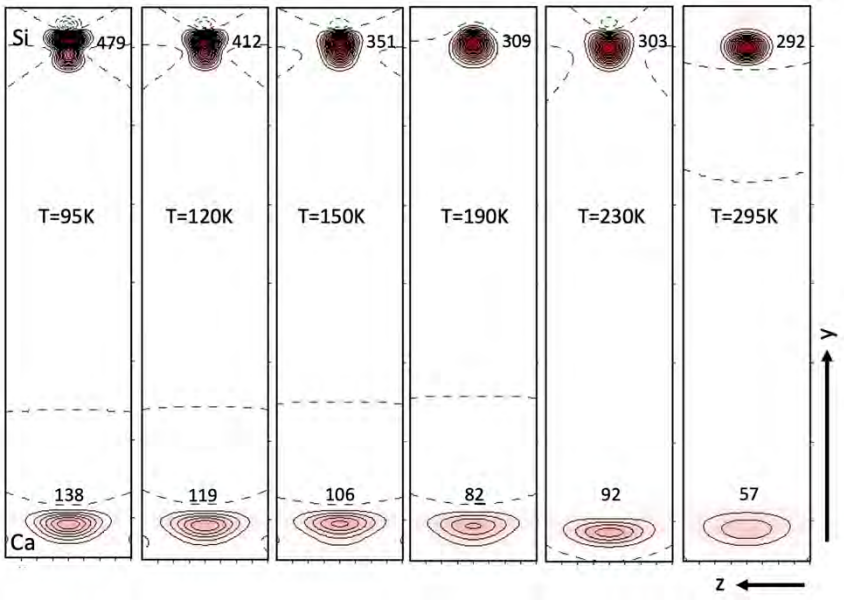

Figure 11: Joint probability density functions of Ca (bottom) and Si (top) between 95K and 295K. Numbers denote the maximum jpdf at both atomic positions. Solid lines mark positive, broken lines negative contour levels in intervals of 20.

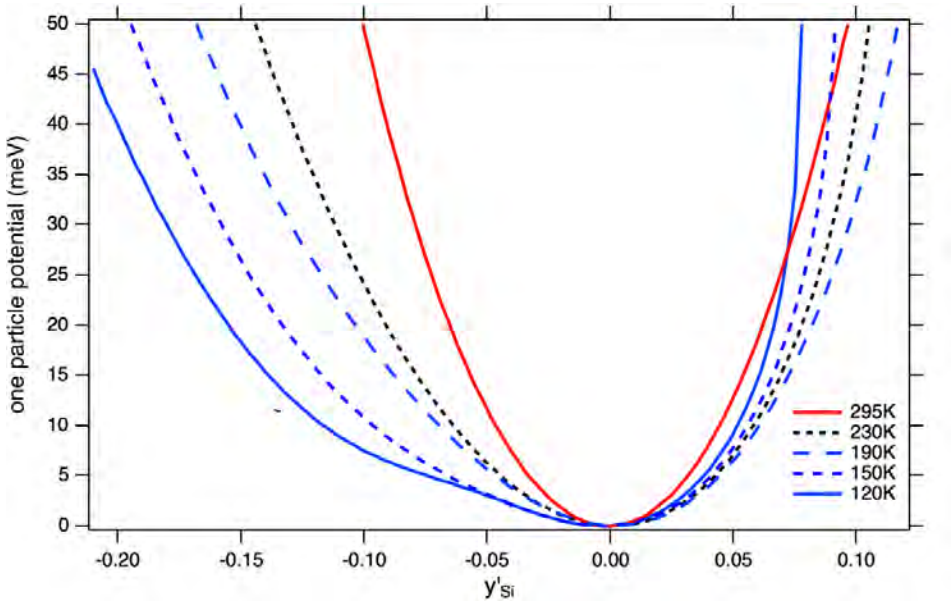

Figure 12: One particle potential of the Si atom parallel to [010] at various temperatures. For clarity all potentials have been shifted to a common minimum, so that y'=0 does not necessarily coincide with the average position of the Si-atom.